metals

MDPI

Article

CMT-Based Wire Arc Additive Manufacturing Using 316L Stainless Steel: Effect of Heat Accumulation on the Multi-Layer Deposits

Seung Hwan Lee

School of Aerospace and Mechanical Engineering, Korea Aerospace University, 76 Hanggongdaehang-ro, Deokyang-gu, Goyang-si, Gyeonggi-do 10540, Korea; seunglee@kau.ac.kr; Tel.: +82-2-300-0106

Received: 3 January 2020; Accepted: 18 February 2020; Published: 20 February 2020

Abstract: CMT welding sources are garnering attention as alternative heat sources for wire arc additive manufacturing because of their low-heat input. A comprehensive experimental and numerical study on the multi-layer deposition of STS316L was performed to investigate effect of heat accumulation during the deposition. The numerical model which is appropriate for WAMM was developed considering the characteristics of the CMT heat source for the first time. Using a high-speed camera, the transient behavior of the CMT arc was investigated, and applied to the heat source of the numerical model. The model was then used to analyze 10-layered deposits of STS316L, fabricated using CMT-based WAAM. During deposition, the temperature is measured using a pyrometer to analyze the microstructure, after which the cooling rate of each layer is estimated. The measured and simulated SDAS were compared. Based on the comparison, a guideline for the equation regarding the SDAS size and cooling rate was suggested.

Keywords: wire arc additive manufacturing (WAAM); heat accumulation; cooling rate; secondary dendrite arm spacing; cold metal transfer (CMT); microstructure; 316L stainless steel

1. Introduction

In additive manufacturing (AM), complex, three-dimensional deposits are manufactured without using moulds, increasing the productivity and manufacturing flexibility compared to traditional manufacturing techniques [1]. Among AM techniques, direct energy deposition (DED) is more advantageous than powder bed fusion (PBF) for manufacturing large parts due to its high deposition rate [1,2]. Wire arc additive manufacturing (WAAM), which is a DED method, is a manufacturing process that involves the melting of the supplied wire using an arc as the heat source, and is a droplet-based AM technique with a fast deposition rate. Compared to powder-based methods, it causes fewer defects, such as pores, enabling the realisation of high-quality products [3,4]. Moreover, most of the heat-source equipment used in WAAM are cheaper compared to laser or electron beam equipment because it uses a conventional commercial welding machine; in addition, the cost of the metal wire used as feedstock is approximately 10% that of the powder [5].

To maximise the benefits of WAAM, it is necessary to understand the microstructure of the deposit which is closely related to the mechanical properties of the AM deposit. Numerous researchers are actively investigating the relationship between the thermal history and microstructure of the deposit. Bintao et al. [6] measured the temperature history of the deposit through a pyrometer in the gas tungsten-WAAM (GT-WAAM) process using Ti-6Al-4V to investigate the changes in the microstructure with respect to the heat accumulation in each layer. Based on the results, it was asserted that with the progress in deposition, the cooling rate decreased due to the increase in heat accumulation, and the width of the α lamellae tended to increase. Jinguo et al. [7] investigated the cooling rate and

microstructure changes based on the height of the deposit in the cold metal transfer-WAAM process using 2Cr13 stainless steel; the authors claimed that the martensite content in the microstructure formed in each layer varied with the differences in the cooling rates of each layer. Asala et al. [8] measured the temperature history during WAAM using Inconel 718, and studied the microstructure variation with respect to the height of the deposit; they observed that the lower and middle parts of the deposit remained for a longer period within the aging-temperature range of Inconel 718 during deposition compared to the upper part, resulting in increased precipitation hardening in the microstructure, thereby demonstrating enhanced mechanical properties.

In order to predict and control the mechanical properties, the thermal characteristics of the deposit need to be simulated for cost saving [9,10]. Few researchers are attempting to simulate the thermal characteristics of WAAM. F. Hejripour et al. [11] used 2209 duplex stainless steel (DSS) to manufacture wall- and tube-shaped deposits with the WAAM process, and developed 3D numerical thermal models to analyse the temperature history and cooling rate of each deposit layer; they stated that ferrite to austenite transformation was promoted, when the cooling rate of each deposit layer was below 50 °C/s. Jun et al. [12] fabricated a circular wall deposit with WAAM using mild steel, and developed a 3D transient heat transfer model; applying this model, they reported that the maximum temperature gradient, when the heat source passes through the centre of the layer during deposition was quantified for each layer.

In the aforementioned study, the thermal characteristics were simulated under various environments. However, none have considered the thermal characteristics of a cold metal transfer (CMT) welding source which has been garnering attention of late as an alternative heat source for WAAM because of its low-heat input.

In view of the above, this study performs a comprehensive experimental and numerical study on the multi-layer deposition of STS316L to investigate effect of heat accumulation. The numerical model which is appropriate for WAMM was developed considering the characteristics of the CMT heat source for the first time. Using a high-speed camera, the transient behavior of the CMT arc was investigated, and this behavior was taken into account for the heat source of the numerical model. For the light model, considering practical applications, a domain-activation method was adopted to analyze the effect of mass flow. Furthermore, to analyze the characteristics of the microstructure of the STS 316L deposit due to heat accumulation produced during WAAM, the temperature at a fixed point in the deposit was continuously measured using a pyrometer. Using the temperature profiles, the measured and simulated secondary dendrite arm spacing (SDAS) were compared to confirm the thermal history at various points of the deposit. Based on this comparison, a guideline for the equation regarding the SDAS size and cooling rate was suggested.

2. Experimental Setup

As shown in Figure 1, the deposit was produced using 1.2 mm diameter STS 316L wire at a single-pass, with multilayers on an STS 316L substrate. The wire used for deposition was M-316L (KISWEL, Seoul, Republic of Korea). Table 1 lists the chemical composition of the substrate and wire. A TPS 4000 CMT welder (FRONIUS, Wels, Austria) was used as the heat source for deposition, which enables relatively low-heat input deposition compared to the other arc welders. For the deposition, STS316L synergetic line and CMT mode were selected. The min and max values for current were 60 A and 250 A, respectively. The average current and voltage were 120 A and 11.2 V, respectively. 100% Ar gas was used as a shielding gas. The details of the process parameters were listed in Table 2.

The XYZ 3-axis automatic motion stage (Six Degrees Inc., Uiwang-si, South Korea) was introduced for deposition path control and process automation for deposition. The specimen being deposited was fixed to the XY stage and moved along the X-axis during deposition; the torch was fixed to the Z-stage and moved along the Z axis.

To observe the temperature history and change in microstructure of the previous layer with respect to the heat accumulation of the deposit because of the deposition of the next layer in WAAM,

the specimens were prepared for each layer at an interpass time (IPT) of 0 s and 60 s, respectively; at these IPTs, 10 test specimens, each, from the 1st–10th layer, were prepared, with a total of 20 test specimens. The average thickness of each layer for IPT 0 s and 60 s were about 1.6 mm and 1.78 mm. The deposition path was zigzag; i.e., deposition was performed by moving 100 mm along the XY stage at a speed of 0.5 m/min in the +X direction, after which the structure was air-cooled during the IPT. Subsequently, deposition was performed moving 100 mm at a speed of 0.5 m/min in the -X direction, after which the structure was again air-cooled during the IPT. This pattern was repeated for the entire deposition.

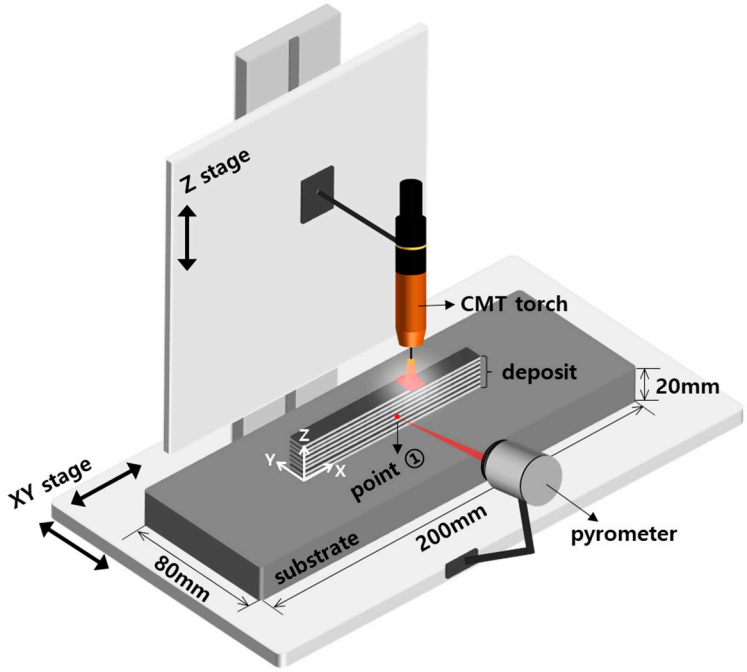

Figure 1. Schematic of the experimental setup.

Table 1. Chemical compositions of the STS 316L wire and substrate.

Materials	Element (wt. %)									
	C	Si	Mn	P	S	Cu	Ni	Cr	Mo	Fe
Wire	0.01	0.59	1.53	0.027	0.001	0.17	11.55	18.56	2.53	Bal.
Substrate	0.016	0.50	1.25	0.030	0.001	0.26	10.09	16.63	2.05	Bal.

Table 2. Process parameters for STS 316L deposition.

Parameter	Value	Parameter	Value
Current [A]	120	Wire feed rate [m/min]	3.6
Voltage [V]	11.2	Shielding gas (Ar) flow rate [L/min]	20
Travel speed [m/min]	0.5	Contact tip to work distance [mm]	10

As depicted in Figure 1, the temperature profile of the deposit during deposition was obtained using a pyrometer (CT Laser 3MH3, OPTRIS, Portsmouth, NH, USA, temperature range: 250–1800 °C). At point ① of Figure 1, the pyrometer measured the temperature of the deposit side (XZ plane) at 50 mm in the +X direction and 3 mm in the +Z direction. The pyrometer was fixed to the XY stage and the XY stage can move only within the horizontal (XY) plane. In other words, the only Z stage can vertically move. As a result, the pyrometer was always looking at one fixed point during the deposition. When measuring the temperature using a pyrometer, the emissivity should be set. To apply an emissivity

suitable for solid state STS316L prior to deposition, calibration experiments were performed to compare the temperature data measured using a K-type thermocouple with that measured using the pyrometer. For the calibration, the K-type thermal couple was attached to one side of an 80 mm thick specimen, and the pyrometer was focused at the same position. The specimen was heated using a gas torch and the temperature data of the thermal couple and the pyrometer were recorded using the NI-DAQ 9229 data acquisition board (NI, Austin, TX, USA). Based on these results, the pyrometer emissivity was set to 0.96 suitable for solid state STS316L.

In addition, the shape of the CMT arc was captured to measure the size of the arc heat-source and estimate the heat flux employed in the simulation model for the first time. An APX-RS high-speed camera (Photron, Tokyo, Japan) was used for arc imaging. Prior to the use of the high-speed camera, a spectral analysis on the CMT arc was performed. Strong emission lines were detected in the range from 520 nm to 550 nm. Thus, a 532 nm bandpass filter was selected and attached to the camera lens to obtain the relatively clear arc shape and to block other spectral bands for the protection of the camera CCD. In addition, a ND filter was used to adjust the brightness of the arc. When the adjusted brightness is exactly same with the contour size of the molten pool in the scanning direction as shown in Figure 2, the adjusted brightness can be defined as the heat source shape because the arc intensity corresponding to the brightness have enough heat energy to melt the metal. Figure 2 displays the droplet transfer in a 17.25 ms cycle. The CMT welder torch controlled the wire feed through a push-and-pull system. Accordingly, during deposition, the arc was repeatedly turned on/off as depicted in Figure 2a–d. From the acquired image, after simplifying the arc shape as shown by the dotted line in Figure 2b, the front (a_f) and rear (a_r) radii of the arc were measured. The arc shapes and heat flux during a total of 10 cycles were obtained and applied to the heat source of the simulation model.

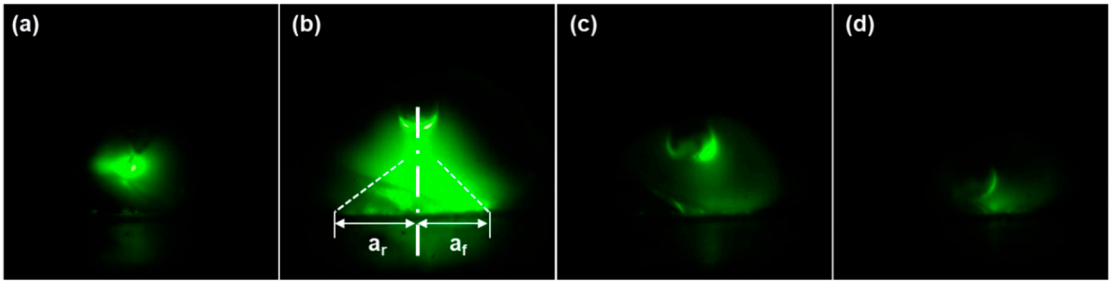

Figure 2. Evolution of the arc captured with a high-speed camera during once cycle (17.25 ms from (**a**–**d**)) of the CMT-based WAAM process.

3. Finite Element Model

A numerical simulation model of the heat transfer was developed to verify the thermal history of the deposit fabricated through the CMT-based WAAM process. For the simulation, a 3D transient heat transfer analysis was performed using a commercial software package, COMSOL Multiphysics 5.2. The developed model does not consider the flow of the molten pool, but considers simple heat transfer alone, including the phase change, as follows:

$$\frac{\partial\left(\rho C_p T\right)}{\partial t} = \frac{\partial}{\partial x}\left(k\frac{\partial T}{\partial x}\right) + \frac{\partial}{\partial y}\left(k\frac{\partial T}{\partial y}\right) + \frac{\partial}{\partial z}\left(k\frac{\partial T}{\partial z}\right) + q, \quad (1)$$

where T is the unknown temperature, C_p is the heat capacity, ρ is the mass density, k is the conductivity, t is the time, and q is the heat input. C_p, ρ, and k are temperature-dependent variables; the values for STS316L were applied with reference to existing literature [13,14]. Furthermore, the latent heat required for phase change was considered by modifying C_p according to the temperature. For the

boundary conditions, the radiation and convection applied to the deposition of the test specimens and the ambient environment are as follows:

$$\mathrm{h} = \frac{\varepsilon\sigma\left(T^4 - T_{amb}^4\right)}{(T - T_{amb})} + h_{con}, \tag{2}$$

where h is the combined heat transfer coefficient comprising radiation and convection, ε is the surface emissivity and σ is the Stefan-Boltzmann constant; T_{amb} is the ambient temperature, which was set to 300 K in this model; h_{con} is the convection coefficient which was applied with reference to existing literature [15]. Adiabatic conditions were applied for the bottom surface of the substrate.

For the heat source applied to the simulation, the double ellipsoid heat source model proposed in Goldak et el. [16] was used [17,18]. The power density distribution of the heat source applied to the radius of the front and rear regions of the arc differs based on the wire center line and is given as follows:

$$q_f = \frac{6\sqrt{3}Qf_f}{\pi\sqrt{\pi}a_f bc}\exp\left[-3\left(\frac{x^2}{a_f^2} + \frac{y^2}{b^2} + \frac{z^2}{c^2}\right)\right], \tag{3}$$

$$q_r = \frac{6\sqrt{3}Qf_r}{\pi\sqrt{\pi}a_r bc}\exp\left[-3\left(\frac{x^2}{a_r^2} + \frac{y^2}{b^2} + \frac{z^2}{c^2}\right)\right], \tag{4}$$

$$f_f + f_r = 2, \tag{5}$$

$$Q = \eta \times V \times I, \tag{6}$$

Here, a is the length of the double ellipsoid, b is the width of the heat source, c is the depth of the heat source, and f is the distribution coefficient. Subscription f and r indicate the front and rear regions of the arc, respectively. Q is the heat input considering the arc efficiency, η is the arc efficiency, and V and I are the voltage and current applied to the deposition process, respectively. The non-symmetric parameters a_f and a_r for the heat source were measured as mentioned in Section 2. Others were cited from the model proposed by Goldak et el. [16]. Table 3 lists the parameters of the employed heat source [16].

Figure 3 displays the shape of the symmetric model and the initial temperature set for the domain activation model used in the FE model. As shown in Figure 3a, the shape of the substrate and the deposit in the model have the same dimensions as those the test specimen. To reduce the computational load of the model, only one symmetric half of the deposit was considered in the XZ plane. A nonuniform mesh scheme was applied to the entire domain. A 0.2 mm fine hexahedron mesh was applied near the heat-source area for the trade-off between computational accuracy and time. In this model, each layer thickness was set to 1.6 mm. As a result, 8 nodes within a layer were located and the 8 nodes were enough for the numerical accuracy from the empirical studies. The entire FE model comprised approximately 126,000 elements.

In addition, to analyze the effect of the mass flow, the domain activation method [11] was used in the simulation, which simplifies the element activation method [13,17]. In AM process analysis, the element activation method is applied to simulate the shape of the deposit that changes in real time due to mass flow. However, during simulation, the computational load becomes extensive because activation and deactivation are performed sequentially for each element. Therefore, in this study, each layer was divided into four equally sized domains considering the computational load [11]. As shown in Figure 3b, for the initial temperature of the activated domain, the temperature calculated in the previous layer was applied.

Table 3. Heat source parameters for the simulation.

Parameter	a_f [mm]	a_r [mm]	b [mm]	c [mm]	f_f	f_r	η	V [V]	I [A]	v [m/min]
Value	7	13	4	4	0.6	1.4	0.85	1.2	120	0.5

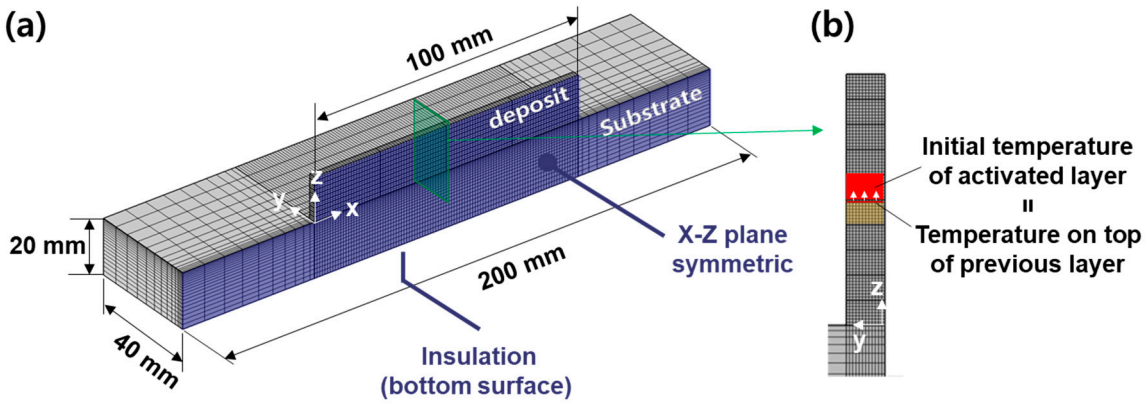

Figure 3. Finite element model for WAAM simulation: (**a**) shape of the symmetric model and (**b**) initial temperature of a new layer.

4. Results and Discussion

4.1. Microstructures

Figure 4 shows the cross-section of the deposit produced using WAAM. Figure 4a and b depict macro cross-section photographs of the deposits with 10 layers under IPT 0 s and 60 s conditions, respectively. When deposition commences, the supplied heat is conducted to the substrate and rapidly dissipates. The higher the deposited layer, the greater is the heat accumulated, and the reduction in the heat dissipation rate is more.

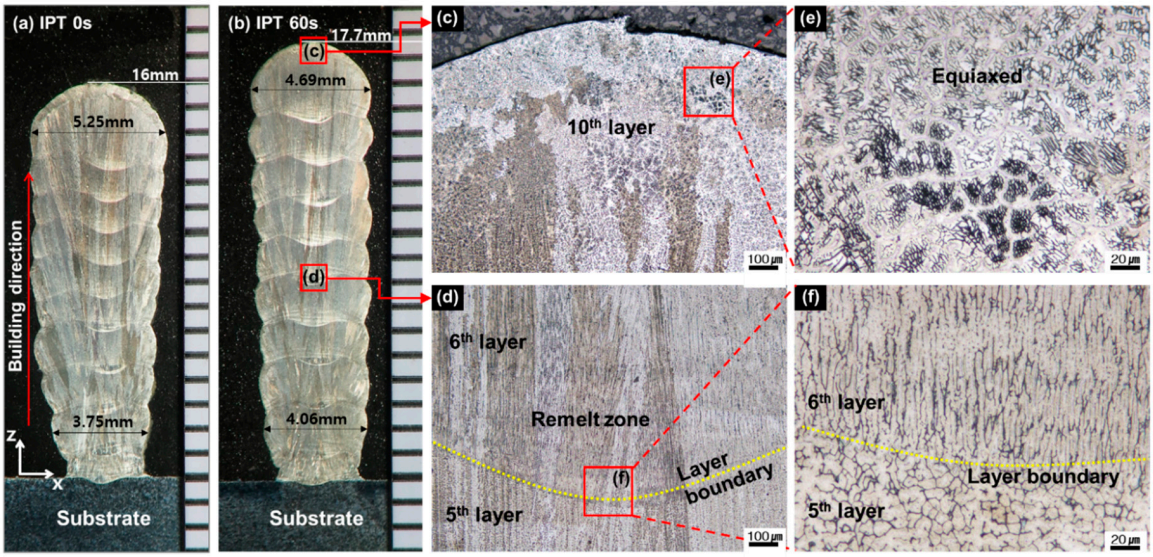

Figure 4. Macro cross-section photograph for (**a**) 0 s IPT and (**b**) 60 s IPT, (**c**) 10th layer (surface) for 60 s IPT, (**d**) layer boundary of 60 s IPT, (**e**) the enlarged micrograph of the surface area, and (**f**) the enlarged micrograph of the boundary.

As illustrated in Figure 4a and b, the grain grows in the +Z direction which is antiparallel to the heat-flow direction. The height of the deposit in Figure 4a under IPT 0 s is 16 mm, whereas that in Figure 4b under IPT 60 s is 17.7 mm. As the deposit in Figure 4a increases from the lower to higher layers, the width of the layer increases, compared to that in Figure 4b. The increase is caused by the viscosity change of the molten metal during the deposition. Viscosity depends on temperature. The viscosity of the molten metal during the deposition decreases as the surrounding temperature increases. In other words, the deposit in Figure 4a has more accumulated heat than that in Figure 4b;

the preheating temperature is high, when the layer is deposited. Therefore, if the viscosity is less, the flow in the width direction can be increased.

Figure 4c is the microstructure photograph of the 10th layer of the deposit under IPT 60 s. An equiaxed structure shown in Figure 4e is created in the surface region on top of the 10th layer because the surface has a relatively faster cooling rate than that within. When the next layer is deposited over the equiaxed structure shown in Figure 4f, a portion of the top layer re-melts, as shown in Figure 4d. As a result, the melted area of the previous layer is approximately 45–60% of the height of the layer. These phenomena were identically observed at the deposit manufactured under IPT 0 s and the microstructure photographs of the deposit under IPT 0 s were omitted.

The Cr equivalent (Cr_{eq}) and Ni equivalent (Ni_{eq}) values were calculated using Equations (7) and (8) of the Schaeffler diagram [19], with the information from Table 1 for the 316L substrate and wire:

$$Cr_{eq} = \%Cr + \%Mo + 1.5 \times \%Si + 0.5 \times \%Nb, \quad (7)$$

$$Ni_{eq} = \%Ni + 30 \times \%C + 0.5 \times \%Mn, \quad (8)$$

Through FE-SEM/EDS analysis as shown in Figure 5, the chemical compositions of the first and second layers of the deposits were measured to check degree of dilution [20]. The calculated Cr_{eq} and Ni_{eq} for the substrate were 19.43 and 11.20, respectively, whereas those for the wire were 21.98 and 13.88, respectively. The values for the 1st layer of the deposit were 19.80 and 11.58, whereas those for the 2nd layer were 20.63 and 11.76, respectively. All the layers including the substrate might form a ferrite-austenite structure with a ferrite content of 5–10 wt. %.

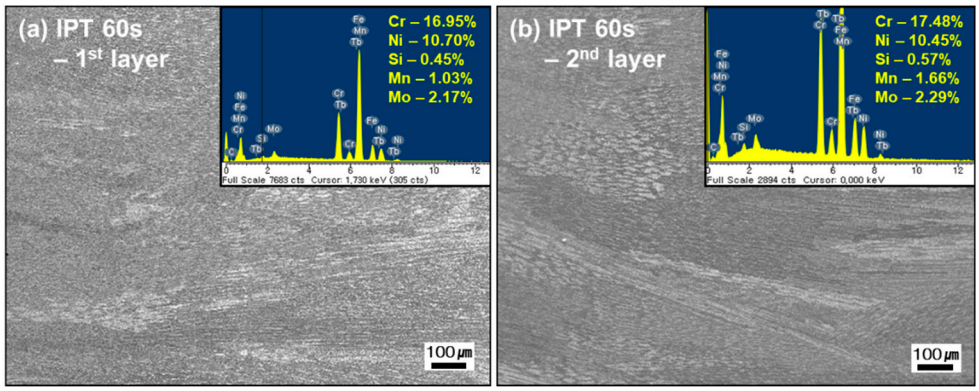

Figure 5. SEM micrographs and SEM-EDS analysis (inset) of 1st (**a**) and 2nd (**b**) layers.

After simplifying the chemical composition of the austenitic stainless-steel elements with Cr_{eq} and Ni_{eq}, the solidification mode of austenitic stainless steel can be predicted using the calculated Cr_{eq} and Ni_{eq}. The solidification mode according to the Cr_{eq}/Ni_{eq} ratio of STS316L, and the type of phase appearing in the mode are schematically expressed in Figure 6. If the Cr_{eq}/Ni_{eq} ratio in the alloy is greater than 1.48 and less than 1.95, the ferrite solidifies in the primary phase and austenite is transformed from Cr, which is the FA mode [17]. The structure is formed as per the following order [9]:

$$L \rightarrow (L + \delta) \rightarrow (L + \delta + \gamma) \rightarrow (\gamma + \delta) \text{ [FA mode]}, \quad (9)$$

where L is the liquid, γ is austenite, and δ is ferrite.

The Cr_{eq}/Ni_{eq} value of the 1st and 2nd layers of the deposit were both 1.75. Cr_{eq}/Ni_{eq} of each layer can be expected to range from 1.58 (wire) $\leq Cr_{eq}/Ni_{eq} \leq$ 1.95. Therefore, each layer of the deposit is expected to solidify through the FA mode in the order shown in Equation (9) and in the red box of Figure 6; the region with low Cr then is converted to austenite at the end of the solidification, leaving a Cr-rich "skeleton" in the dendrite core. As predicted, after solidification, a microstructure of austenite + skeletal ferrite was observed in most of deposits, as shown in Figure 7.

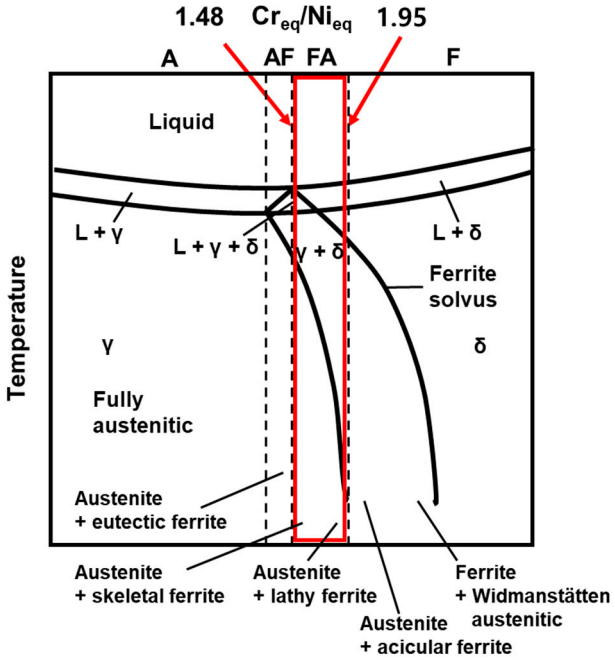

Figure 6. Relationship between the solidification type and the pseudo-binary phase diagram for austenitic stainless steel [21].

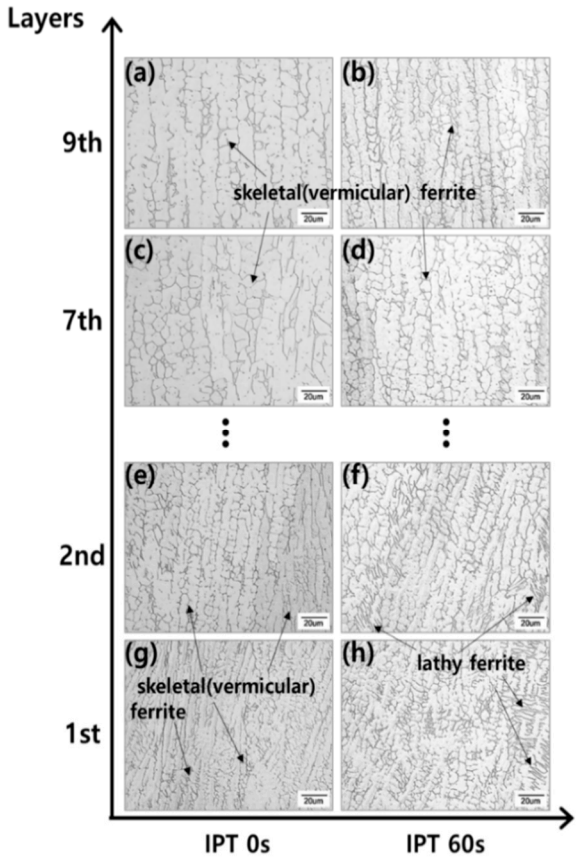

Figure 7. Optical-microscope images of the microstructure with respect to the IPT for STS 316L (**a**) 9th layer for 0 s IPT; (**b**) 9th layer for 60 s IPT; (**c**) 7th layer for 0 s IPT; (**d**) 7th layer for 60 s IPT; (**e**) 2nd layer for 0 s IPT; (**f**) 2nd layer for 60 s IPT; (**g**) 1st layer for 0 s IPT; (**h**) 1st layer for 60 s IPT.

In addition, as depicted in Figure 7f and h, lathy ferrite was found in certain portions of the deposits, in agreement with that depicted in the red box of Figure 7. As shown in Figure 7, columnar dendrite morphology was observed in each layer of the deposit. The SDAS details will be discussed in the next section.

4.2. Experimental Validation Using the Numerical Model

Figure 8 shows the temperature profile measured at a fixed spot on the deposit (point ① depicted in Figure 1) during the deposition of the 1st–10th layers. The temperature profiles at the deposits produced under IPTs of 0 s and 60 s were compared with the temperature profiles calculated in the simulation using the model described in Section 3.

In Figure 8a and b, although the peak temperatures obtained from the experiment and simulation have negligible differences, the cooling rates which are the slopes of the profiles after the peak temperature, are nearly identical. The maximum temperatures in the 2nd and 3rd layers in the simulation were greater than the maximum temperature measured by the pyrometer. This is mainly caused by the emissivity, which is one of the set values of the pyrometer. As the emissivity of the pyrometer was set for the solid phase of STS316L, the temperature of the liquid phase cannot be detected. When the CMT torch passed over the point ①, the point ① where the pyrometer is observing temporally has the mixed phases of solid and liquid during the solidification. The measurements of maximum temperatures in the 2nd and 3rd were affected by these two phases because the point ① was located near the 2nd and 3rd layers. Therefore, due to the error induced by the emissivity of the two phases, the peak temperatures expressed by the black lines exhibited dual peaks at approximately 1200 °C or do not exceed approximately 1200 °C. The average errors of the other peak temperatures, between the simulation and experiments, under the two IPT conditions were approximately 8.33% and 8.16%, respectively.

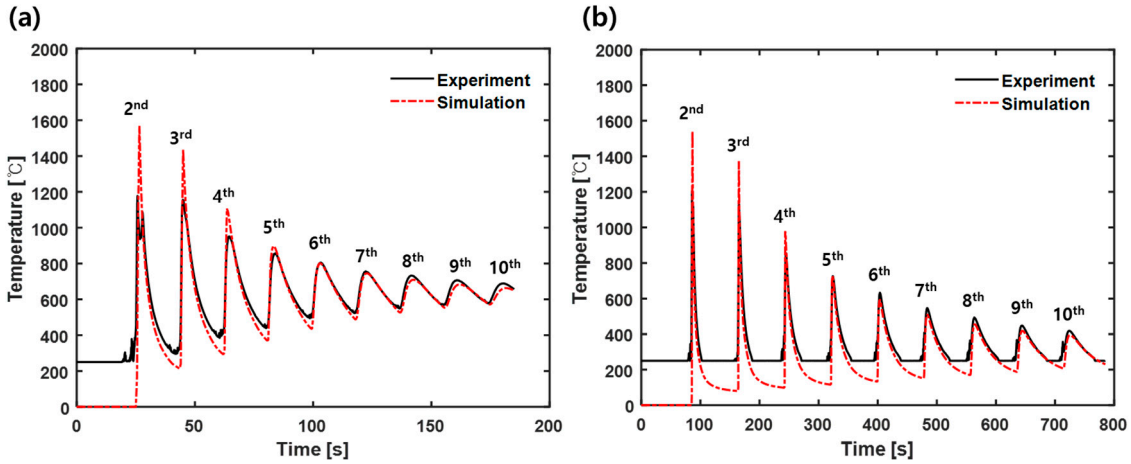

Figure 8. Comparison of the simulated and experimental results for the temperature history of 10-layer deposits at: (**a**) point ① under 0 s IPT and (**b**) point ① under 60 s IPT.

Using the temperature profiles, the measured and simulated SDAS were compared to confirm the thermal evolution of the deposits because SDAS is an important index to evaluate the deposits in the WAMM [10,22,23]. The SDAS of each layer of the deposit shown in Figure 7 was measured. The simulated SDAS was obtained using Equation (10) [24]:

$$\lambda_2 = 50(GR)^{-0.4} \quad (10)$$

where λ_2 is the SDAS in μm and GR is the cooling rate in K/s. Equation (10) indicates that the SDAS increases as the cooling rate decreases.

Using the numerical model, the cooling rate of each layer depending on the IPT conditions were simulated as shown in Figure 9a. The cooling rates were calculated at the centre of each layer in the YZ plane near point ①. The cooling rate exponentially decreased in both cases. However, due to heat accumulation, the cooling rate of the 60 s IPT was considerably high more than that of the 0 s IPT. In addition, the cooling rates at the low-level layers were greater than those of the higher ones.

Figure 9b compares the simulated SDAS with the measured SDAS in each layer. In layers excluding the 1st and 2nd, the SDAS of the deposit under 0 s IPT was greater than those of the deposit under 60 s IPT, and the SDAS size slowly increased after the 4th layer in both conditions. This phenomenon can be explained as follows: (i) after the previous layer is deposited, and before the deposit is cooled to room temperature (300 K), the deposition of the next layer commences; in the test specimen under 0 s IPT, more heat is accumulated and the cooling rate slows down; (ii) the 4th–10th layers slowly cools down compared to the 1st–3rd layers.

As shown in Figure 9b, the simulated SDAS based on Equation (10) fit the measured SDAS well until the 7th layer. However, the difference between the measured and simulated SDAS under 0 s IPT starts to increase from the 7th layer. The difference indicates that Equation (10) fit better in higher cooling rate. In other words, the critical cooling rate can be considered to about 50 K/s corresponding to the 7th layer under 0 s IPT.

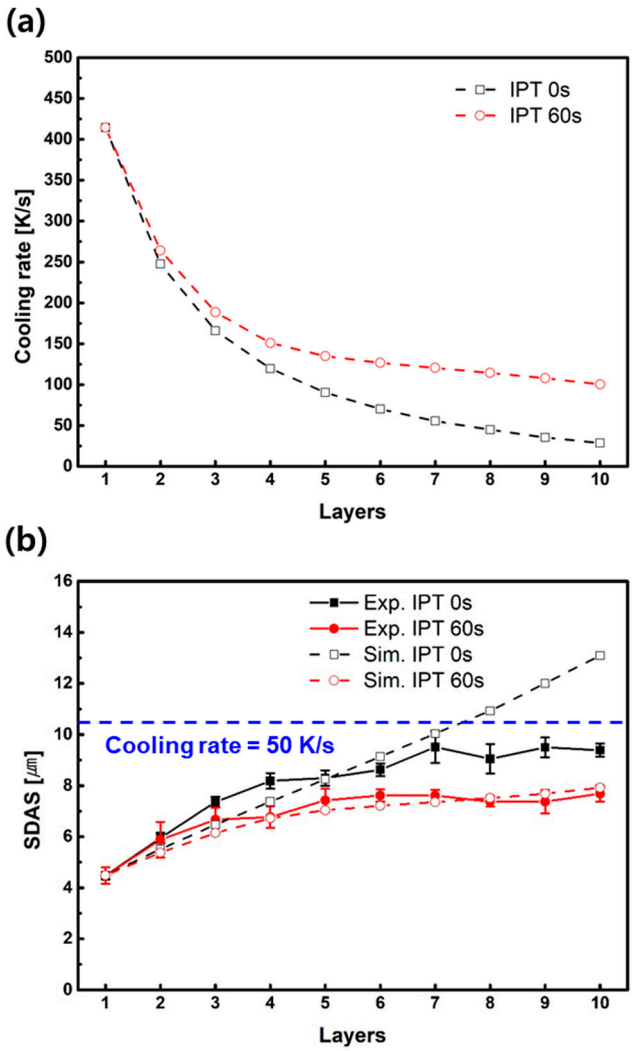

Figure 9. Relationship between the cooling rate and SDAS under IPTs of 0 s and 60 s: (**a**) Simulated cooling rate, and (**b**) measured (experiment) and simulated SDAS (simulation).

This result agrees with the literature [24]. Equation (10) was originally suggested using a simulation result and validated with experimental data of other literatures; when the cooling rate was low, about 40 K/s, the validated SDAS have 30% error with the simulation result. However, in the higher cooling rate above the 40 K/s, the simulation results were more accurate.

In addition, in this study, the simulation model was validated from the directly measured temperature of the deposit using the pyrometer rather than the indirectly measured temperature of the base metal using thermo-couples. Therefore, Equation (10) is recommended to use in higher cooling rate, especially over a cooling rate of 50 K/s.

5. Conclusions

In this study, a comprehensive experimental and numerical study on the multi-layer deposition of STS316L was performed to investigate effect of heat accumulation during the deposition. The salient conclusions are as follows:

(1) The numerical model which is appropriate for WAMM was developed considering the characteristics of the CMT heat source for the first time. Using a high-speed camera, the transient behavior of the CMT arc was investigated, and this behavior was taken into account for the heat source of the numerical model. For the light model, considering practical applications, a domain-activation method was firstly adopted to analyze the effect of mass flow in the WAMM. In addition, a ND filter was used to adjust the brightness of the arc and the adjusted brightness was used for the realistic value of Goldak's model. As a result, during cooling after depositions, the simulated and measured temperature show almost identical profiles except the peak temperatures with about 8% error. This work can directly be applied to various shapes of deposits for the thermal analysis.

(2) Macro and micro characteristics of the deposits were comprehensively investigated. Especially, IPT was considered for the analysis of the heat accumulation during the multi-layer depositions. When a new layer was deposited over the top(previous) layer, due to the differences in the preheating temperature of the previous layer depending on IPT, approximately 45–60% of the top layer was found to be re-melt. In addition, the measured and simulated SDAS of the deposits were compared to investigate the heat accumulation. As a result, the equation regarding the SDAS size and the cooling rate was found to be more accurate over cooling rate of 50 K/s. From this result, mechanical properties such as hardness and yield strength in the WAMM can be anticipated to predict.

Funding: This work was supported by the National Research Foundation of Korea (NRF) grant funded by the Korea government (MSIT) (No. 2017R1C1B5018334) and by the Korea Evaluation Institute of Industrial Technology (KEIT) grant funded by the Korea government (MOTIE) (No. 20000258).

Conflicts of Interest: The authors declare no conflict of interest.

References

1. Lee, Y.; Kirka, M.M.; Dinwiddie, R.B.; Raghavan, N.; Turner, J.; Dehoff, R.R.; Babu, S.S. Role of scan strategies on thermal gradient and solidification rate in electron beam powder bed fusion. *Addit. Manuf.* **2018**, *22*, 516–527. [CrossRef]
2. Chen, X.; Li, J.; Cheng, X.; Wang, H.; Huang, Z. Effect of heat treatment on microstructure, mechanical and corrosion properties of austenitic stainless steel 316L using arc additive manufacturing. *Mater. Sci. Eng. A* **2018**, *715*, 307–314. [CrossRef]
3. Biswal, R.; Zhang, X.; Syed, A.K.; Awd, M.; Ding, J.; Walther, F.; Williams, S. Criticality of porosity defects on the fatigue performance of wire+ arc additive manufactured titanium alloy. *Int. J. Fatigue* **2019**, *122*, 208–217. [CrossRef]
4. Szost, B.A.; Terzi, S.; Martina, F.; Boisselier, D.; Prytuliak, A.; Pirling, T.; Hofmann, M.; Jarvis, D.J. A comparative study of additive manufacturing techniques: Residual stress and microstructural analysis of CLAD and WAAM printed Ti–6Al–4V components. *Mater. Des.* **2016**, *89*, 559–567. [CrossRef]

5. Ziętala, M.; Durejko, T.; Polański, M.; Kunce, I.; Płociński, T.; Zieliński, W.; Łazińska, M.; Stępniowski, W.; Czujko, T.; Kurzydłowski, K.J. The microstructure, mechanical properties and corrosion resistance of 316 L stainless steel fabricated using laser engineered net shaping. *Mater. Sci. Eng. A* **2016**, *677*, 1–10. [CrossRef]
6. Wu, B.; Pan, Z.; Ding, D.; Cuiuri, D.; Li, H. Effects of heat accumulation on microstructure and mechanical properties of Ti6Al4V alloy deposited by wire arc additive manufacturing. *Addit. Manuf.* **2018**, *23*, 151–160. [CrossRef]
7. Ge, J.; Lin, J.; Lei, Y.; Fu, H. Location-related thermal history, microstructure, and mechanical properties of arc additively manufactured 2Cr13 steel using cold metal transfer welding. *Mater. Sci. Eng. A* **2018**, *715*, 144–153. [CrossRef]
8. Asala, G.; Khan, A.K.; Andersson, J.; Ojo, O.A. Microstructural Analyses of ATI 718Plus®Produced by Wire-ARC Additive Manufacturing Process. *Metall. Mater. Trans. A* **2017**, *48*, 4211–4228. [CrossRef]
9. Kou, S. *Welding Metallurgy*; Wiley: Hoboken, NJ, USA, 2003.
10. Huang, Y.; Ansari, M.; Asgari, H.; Farshidianfar, M.H.; Sarker, D.; Khamesee, M.B.; Toyserkani, E. Rapid prediction of real-time thermal characteristics, solidification parameters and microstructure in laser directed energy deposition (powder-fed additive manufacturing). *J. Mater. Process. Technol.* **2019**, *274*, 116286. [CrossRef]
11. Hejripour, F.; Binesh, F.; Hebel, M.; Aidun, D.K. Thermal modeling and characterization of wire arc additive manufactured duplex stainless steel. *J. Mater. Process. Technol.* **2019**, *272*, 58–71. [CrossRef]
12. Xiong, J.; Li, R.; Lei, Y.; Chen, H. Heat propagation of circular thin-walled parts fabricated in additive manufacturing using gas metal arc welding. *J. Mater. Process. Technol.* **2018**, *251*, 12–19. [CrossRef]
13. Jayanath, S.; Achuthan, A. A Computationally Efficient Hybrid Model for Simulating the Additive Manufacturing Process of Metals. *Int. J. Mech. Sci.* **2019**, *160*, 255–269. [CrossRef]
14. Setien, I.; Chiumenti, M.; van der Veen, S.; San Sebastian, M.; Garciandía, F.; Echeverría, A. Empirical methodology to determine inherent strains in additive manufacturing. *Comput. Math. Appl.* **2019**, *78*, 2282–2295. [CrossRef]
15. Ding, J.; Colegrove, P.; Mehnen, J.; Ganguly, S.; Almeida, P.S.; Wang, F.; Williams, S. Thermo-mechanical analysis of wire and arc additive layer manufacturing process on large multi-layer parts. *Comput. Mater. Sci.* **2011**, *50*, 3315–3322. [CrossRef]
16. Goldak, J.; Chakravarti, A.; Bibby, M. A new finite element model for welding heat sources. *Metall. Trans. B* **1984**, *15*, 299–305. [CrossRef]
17. Oyama, K.; Diplas, S.; M'hamdi, M.; Gunnæs, A.E.; Azar, A.S. Heat source management in wire-arc additive manufacturing process for Al-Mg and Al-Si alloys. *Addit. Manuf.* **2019**, *26*, 180–192. [CrossRef]
18. Wu, Q.; Mukherjee, T.; Liu, C.; Lu, J.; DebRoy, T. Residual stresses and distortion in the patterned printing of titanium and nickel alloys. *Addit. Manuf.* **2019**, *29*, 100808. [CrossRef]
19. Schaeffler, A.L. Constitution diagram for stainless steel weld metal. *Metal Prog.* **1949**, *56*, 680.
20. Abe, T.; Sasahara, H. Dissimilar metal deposition with a stainless steel and nickel-based alloy using wire and arc-based additive manufacturing. *Precis. Eng.* **2016**, *45*, 387–395. [CrossRef]
21. Lippold, J.C.; Kotecki, D.J. *Welding Metallurgy and Weldability of Stainless Steels*; Wiley: Hoboken, NJ, USA, 2005.
22. Wang, L.; Xue, J.; Wang, Q. Correlation between arc mode, microstructure, and mechanical properties during wire arc additive manufacturing of 316L stainless steel. *Mater. Sci. Eng. A* **2019**, *751*, 183–190. [CrossRef]
23. Knapp, G.; Mukherjee, T.; Zuback, J.; Wei, H.; Palmer, T.; De, A.; DebRoy, T. Building blocks for a digital twin of additive manufacturing. *Acta Mater.* **2017**, *135*, 390–399. [CrossRef]
24. Yin, H.; Felicelli, S.D. Dendrite growth simulation during solidification in the LENS process. *Acta Mater.* **2010**, *58*, 1455–1465. [CrossRef]